fortune Journals

Research Article

INTERNATIONAL JOURNAL OF PLANT, ANIMAL AND ENVIRONMENTAL SCIENCES
ISSN: 2231-4490

Thermal Energy Conversion Using NITI Shape Memory Alloy Material

Rabiu Ahamd Abubakar[1*] and Nuhu Ibrahim[2]

Abstract

In this paper, a NiTi SMA heat engine is proposed. It converts thermal energy from a source of temperature different to mechanical energy. The Assumed temperature difference is (70°C). The temperature is obtainable when the engine is used in a geothermal source. But if the engine is used for ocean thermal energy, incorporated solar or heat pumped will be used. The engine behavior is simulated, and the model is compared to experimental data. The engine developed a maximum driving force of 17.3N, a torque of 0.9Nm, and an efficiency of 4.51%.

Keywords: NiTi SMA; Thermomechanical; Phase transformation; Heat engine

Introduction

Thermal energy is a form of energy that occurs by temperature difference [1]. It can also be defined as the energy possessed by an object due to the particle movements within the object. It is the kinetic energy of an object due to random movements of the body molecules and atoms. It occurs naturally in many different kinds like ocean thermal energy caused by the direct sunlight radiation conversion to heat energy [2,3], and geothermal energy [4,5], which naturally occurs beneath the earth crust. Many technologies are used to convert such thermal energy to generate electricity for human and industrial use. Ocean energy has existed since earth creation. It recently attracted research attention for the possible harvesting and used as an alternative source of green energy. Ocean thermal energy occurs due to the temperature differences between the ocean depth and surface [6], usually (100m). Energy demand is increasing every day, and the energy depends on is mostly non-renewable and depleting every day. These energy sources include the following: petroleum, firewood, solar [2,3] biomass [7-9], hydropower [10,11], nuclear, coal, wind [12,13] and many more [14-18]. These energy sources [19] are dangerous to our environment due to harmful carbon footprint emissions [20]. Therefore, alternative, cheaper, safer, and renewable sources are welcome [21,22]. In our ecosystem, different energy sources exist. Hence, converting these energies would help our domestic and industrial activities [23].

Sixty percent of this energy is at 100°C or less[21]. Solar radiation is closed to 8×10^{16}watt energy flux, with 70% heating like sea and ocean, which may be converted to usable energy when explored carefully [24]. Ocean thermal Energy (OTE) is one of these types that can be converted to mechanical energy [25]. OTE is the second largest (1000TW/a) [26] and is stable at low temperature [23]. This can be harvested using the NiTi SMA Heat engine. This will give additional energy sources and help control carbon emissions [27-29]. The temperature difference between the ocean bottom, which is cold, and its top can cause austenite-martensite phase transformation

Affiliation:

[1]Institute of Mechanical engineering Design, Mechanical Engineering Department, Zhejiang University, Hangzhou, China

[2]Centre for Renewable Energy Research. Umaru Musa Yar'adua University Katsina, Katsina state Nigeria

***Corresponding author:**
Rabiu Ahamd Abubakar, Institute of Mechanical engineering Design, Mechanical Engineering Department, Zhejiang University, Hangzhou, China.

Citation: Rabiu Ahamd Abubakar, Nuhu Ibrahim. Thermal Energy Conversion Using NITI Shape Memory Alloy Material. International Journal of Plant, Animal and Environmental Sciences. 14 (2024): 20-30

Received: May 16 2024
Accepted: May 30, 2024
Published: June 06, 2024

Abu-Kharma M, Int J Plant Anim Environ Sci 2024
DOI:10.26502/ijpaes.4490161

that will result in thermos-mechanical energy conversion for electricity generation [25].

Many devices are used for thermos-mechanical energy conversion, but they are not up to the level of commercialization. Research on the Rankine cycle has been recently used for ocean thermal energy conversion. A low boiling medium is used. The Rankine cycle uses a low boiling medium which requires a small temperature difference. It can be used in a tropical region where large solar is converted to thermal energy [2,3], thus warming the ocean water to 28-35°C [30]. Rankine cycle technology has very low efficiency due to the following reason. Because of the low-temperature difference, the process of heat exchange is very restricted. This technology needs a large amount of water to be pumped up from the bottom of the sea to the top. This requires energy, and the pipe needs thermal insulation. Parasite tends to grow on the heat exchanger; thus, it has to clean up from time to time, and all this is energy demanding, which will be very difficult. This makes the Rankine cycle technology inefficient, therefore, it makes it unsustainable due to energy loss.

There is an alternative to the problems mentioned above associated with Rankine technology. That is by applying NiTi SMAs for the energy conversion. NiTi SMA has an outstanding shape memory effect (SME) behavior, which results in thermos-mechanical energy conversion through martensitic phase transformation. Since its invention, there have been many attempts to apply it in energy harvesting, yet it is not up to the level of commercialization [31,32].

A synchronized pulley SMA heat engine is proposed. The engine has two actives pulley and two idle pulleys. Two-timing gears are mounted on the acting pulleys with a synchronizing timing belt.

This research intends to convert both ocean thermal and geothermal energy based on phase transformation.

Research shows that there are synchronized and unsynchronized SMA pulley heat engines [33-35]. In the synchronized type the, due to synchronization, the development resolved to ease tension, so it favors ratio in one direction [36,37]. In unsynchronized pulley type, each pulley rotates independently.

The Conceptual Design and Kinematics

It can be used as an ocean thermal energy harvester or a geothermal energy harvester. The active pulleys are Pulleys 1 & 2 and have the same radius a. SMA spring makes contact wrap angle ϕ. The timing belt connects the two active pulleys. Pulley 3 & 4 are idle pulleys. When using the engine as an ocean energy harvester, the pulley 3 is immersed in bathwater, simulating the ocean surface top, while pulley4 is in a cold-water chamber, simulating the cold ocean bottom. When used as a geothermal energy harvester, the pulley 3 is left in the open air or immersed in cold water simulating the low-temperature sink, while pulley 4 is immersed in a hot water chamber simulating the hot water from the earth crust. An opposing external load like an alternator can be mounted on pulley 2. The SMA spring has F_{CD} in cold water and in hot water, it has $F+\Delta F$. The gear for synchronization has unequal radii b_1 and b_2. The timing belt on top has F_t and on the bottom, $F_t+\Delta F_t$. Assuming no frictional force and no sliding on the pulleys, then Eq. 1 obtained as:

$$M_{load}+b_1\Delta F_t = a\Delta F \quad (1)$$

$$b_2\Delta F_t = a\Delta F \quad (2)$$

Where M_{load} is the external load, a is the radius of the pulley1 & 2, b_1 is the radius of timing gear1 on, and b_2 is the radius of timing gear 2. Using equilibrium equations ΔF_t is eliminated, resolving into a single equation 3.

$$M_{load} = a\Delta F_s\left(1-{b_1}/{b_2}\right) \quad (3)$$

The ratio b_1/b_2 is ($0< b_1/b_2<1$). This restoring SMA spring force is a function of temperature as:

$$\Delta F_s = f(T) \quad (4)$$

In this research, the SMA Spring is made to acquire the shape memory effect through heat treatment. The critical austenite to martensite transformation temperature is set at 30°C. This means if the spring is extended and heated, it will instantly return to its original shape at 30°C. An SMA wire with 1.5 mm diameter is wound around a cylindrical rod of 16mm, then put in a heating furnace and heated up to 500°C for 30 minutes. It is brought out and cooled at ambient temperature. This process sets the SMA spring to the above critical temperature of 30°C [38-41].

Figure 1 shows the SMA spring with installation length L and initial length L_o

$$L = L_{AB}+L_{CD}+2\left(2\pi a\frac{\phi}{360}\right) \quad (5)$$

$$\frac{L}{L_0} = x_0 = \frac{1}{L}\int_0^L x(s)\,ds \quad (6)$$

$$L_0 = V_0(t_B+t_D-t_C)+\left(2\pi a\frac{\phi}{360}\right)\left(x_1^{-1}+x_2^{-1}\right) \quad (7)$$

Where x_0 is the initial stretch ratio.

The Relationship between Temperature and Time

SMA depends largely on the shear modulus (G) of the material. Therefore G has the following relationship with temperature (T):

$$\begin{aligned} &G = G_M \quad when\, T < M_f \,and\, T < A_s \\ &G = G_M \quad when\, T < M_f \,and\, T < A_s \\ &G = G(\lambda, T) \;\; when\, M_f \le T \le A_f \\ &G = G_A \quad when\; T > A_f \,and\, T > M_s \end{aligned} \quad (8)$$

Abu-Kharma M, Int J Plant Anim Environ Sci 2024
DOI:10.26502/ijpaes.4490161

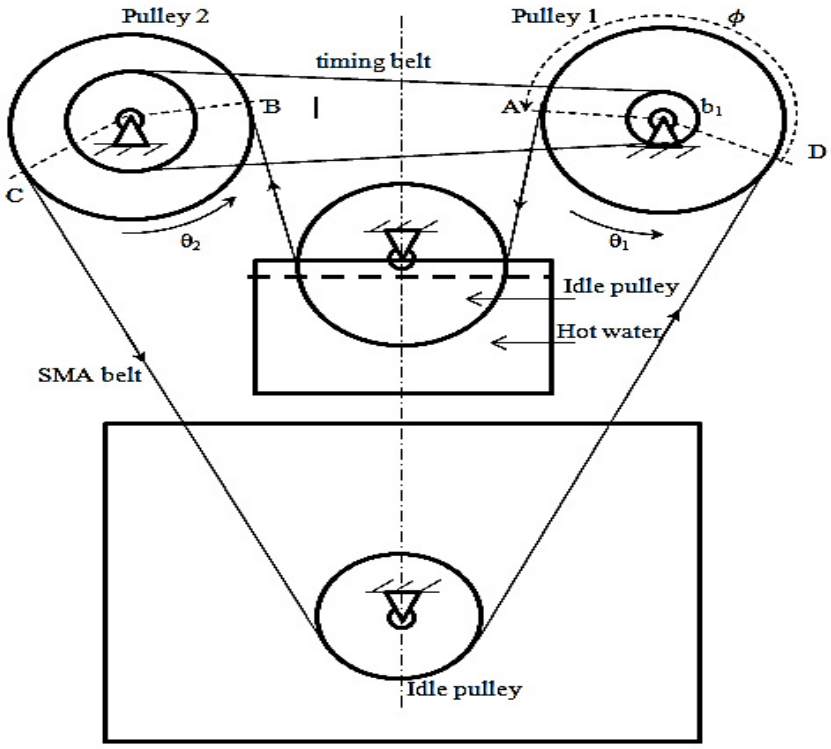

Figure 1: Represents a thermo-mechanical energy converter.

where, *Ms, M_f, As, A_f,* represent the start and finish martensite and austenite temperature. G_A and G_M are the austenite and martensite shear modulus, respectively. In the absence of stress, when: ($M_f \le T \le A_f$), the SMA shear modulus is:

$$G\left(T_{heating}\right)=G_M+\left(\frac{G_A-G_M}{2}\right)\left[1+\sin\Phi(T-T_m)\right] \quad (9)$$

$$G\left(T_{cooling}\right)=G_M+\left(\frac{G_A-G_M}{2}\right)\left[1+\sin\Phi(T-T_m)\right] \quad (10)$$

Therefore during heating

$$T_m=\frac{A_s+A_f}{2},\ \Phi=\frac{\pi}{A_f-A_s} \quad (11)$$

And during cooling,

$$T_m=\frac{M_s+M_f}{2},\ \Phi=\frac{\pi}{M_f-M_s} \quad (12)$$

When the SMA spring is heated, the equation for heat balance is an ordinary differential equation:

$$m'\left(C_s-\Lambda\frac{x_2-x_1}{x_M-x_A}\right)V\frac{dT}{dt}=-H_hA\left(T-T_w\right) \quad (13)$$

Where m' is the SMA Spring mass linear density, C_s is SMA spring specific capacity, V is its total volume, H_h is coefficient of heat exchange A SMA spring surface area, and T_w is water temperature.

When $T=T_0$, at $t=0$, then the temperature variation of SMA spring with time is:

$$T=\left(T_0-T_w\right)e^{-t/\varphi}+T_w \quad (14)$$

Where T_0 is the initial temperature and φ is the time constant of SMA spring,

$$\varphi=\frac{m'\left(C_s-\Lambda\frac{x_2-x_1}{x_M-x_A}\right)V}{H_hA} \quad (15)$$

The Force Generation

The following numbers of turns are observed associated with the engine: n_1 is SMA spring number of turns in AB region, n_2 is SMA spring number of turns in the CD region. Assuming and the stretch ratio (x_1/x_2) of 1:3 is used.

$$n_1=\frac{L_{AB}}{3P_0} \quad (16)$$

$$n_2=\frac{L_{CD}}{3P_0} \quad (17)$$

$$L_{AB}=V_0\int_0^{t_B}x_{AB}(t)\,dt \quad (18)$$

Where n_1 and n_2 are the numbers of turns of SMA spring in the heating and cooling chamber, respectively; L_{AB} and L_{CD} are the length of AB and CD.

When $M_f \le T_2 \le A_f$, the force developed in hot water can be expressed as:

$$F_{AB}(T)=\frac{L_{AB}\left(T_{heating}\right)G\left(T_{heating}\right)}{L_{AB}\left(T_c\right)G_L}F_{AB}\left(T_c\right) \quad (19)$$

And the axial force at a low temperature of cold water can be expressed as:

$$F_{AB}(T_c)=\frac{L_{AB}(T_c)(d_w)^4 G_L}{8(D_s)^3 n_1} \quad (20)$$

Where T_c is the temperature at cold water before heating.

Therefore,

$$F_{AB}(T)=\frac{L_{AB}(T_{heating})(d_w)^4 G(T_{heating})}{8(D_s)^3 n_1} \quad (21)$$

The axial displacement is restricted since the SMA spring acts as a belt with a head-to-tail connection. Therefore, the length of the SMA spring remains the same.

Therefore,

$$L_{AB}(T_{heating})=L_{AB}(T_c) \quad (22)$$

$$F_{AB}(T)=\frac{L_{AB}(T_c)(d_w)^4 G(T_{heating})}{8(D_s)^3 n_1} \quad (23)$$

The axial load developed during cooling is expressed as:

$$F_{CD}(T)=\frac{L_{CD}(T_c)(d_w)^4 G(T_{cooling})}{8(D_s)^3 n_2} \quad (24)$$

Where D is the SMA spring diameter, d_w is the SMA wire diameter, and G_L is the shear moduli of SMA spring at low temperature.

Torque

The engine driving force is:

$$\Delta F_s = F_{AB}(T_{heating})-F_{CD}(T_{cooling}) \quad (25)$$

From Equation 3, the torque/moment generated is:

$$M_{load}=a\left(\frac{L_{AB}(T_c)G(T_{heating})}{n_1}-\frac{L_{CD}(T_c)G(T_{cooling})}{n_2}\right)\left(\frac{(d_w)^4}{8(D_s)^3}\right)\left(1-b_1/b_2\right) \quad (26)$$

The Engine Speed

The angular acceleration is gotten as:

$$\ddot{\theta} I_e = \Delta F_s \times a \quad (27)$$

$$\ddot{\theta}=\frac{\Delta F_s \times a}{I_e} \quad (28)$$

Where I_e is the effective mass moment of inertia of the pulley But, the moment of inertia of the pulley is:

$$I_e=\frac{1}{2}ma^2 \quad (29)$$

where m is the mass of the pulley with radius a.

Therefore,

$$\ddot{\theta}=\frac{2\times\Delta F_s\times a}{ma^2}=\frac{2\times\Delta F_s}{ma} \quad (30)$$

To get the angular velocity, Eqt. 30 is integrated with respect to time.

$$\int\ddot{\theta}=\frac{2}{ma}\int\Delta F_s dt \quad (31)$$

$$\dot{\theta}=\frac{2}{ma}\Delta F_s t + C \quad (32)$$

Where C is the constant of integration, and is here taken as zero. Hence Eq. 32 reduced to:

$$\dot{\theta}=\frac{2}{ma}\Delta F_s t \quad (33)$$

Substituting Eqt. 24 in 29,

$$\dot{\theta}=\frac{2}{ma}\left(\frac{L_{AB}(T_c)G(T_{heating})}{n_1}-\frac{L_{CD}(T_c)G(T_{cooling})}{n_1}\right)\left(\frac{(d_w)^4)}{8(D_s)^3 n_2}\right)t \quad (34)$$

The *T(t), x(t),* and *F(t)* are periodic. And period is:

$$\tau=\frac{2\pi}{\dot{\theta}} \quad (35)$$

From experimental data, pulley1 has 14rpm; therefore, the engine period τ is 4.3s.

Under engine steady operation, there is zero acceleration and no slippage on the pulley, hence there is constant mass flow rate. Let the reference and current velocity be V_o and V, then the linear mass density is:

$$\dot{m}=V_0\frac{dm}{dS}=V(s)\frac{dm}{ds}=constant \quad (36)$$

$$V(s)=V_0 x(s) \quad (37)$$

Therefore at point B and D, the mass flow is as:

$$\dot{m}_B=\frac{a\dot{\theta}_1\frac{dm}{dS}}{x_1}=\dot{m}_D=\frac{a\dot{\theta}_2\frac{dm}{dS}}{x_2} \quad (38)$$

Where $\dot{\theta}_i$ is rotation speed, x_1 and x_2 are the stretch ratio. The timing ratio $\bar{b}$ is expressed as:

$$\bar{b}=\frac{x_2}{x_1} \quad (39)$$

$$b_1\dot{\theta}_1=b_2\dot{\theta}_2 \quad (40)$$

Using parameters in Table 1, Figure 2(a) shows the nonlinear relationship between the force generated versus temperature. As the heating starts, the curve goes nonlinearly from 20 to 30C, and then it goes linearly up to around 60°C and then ends nonlinearly from 60 to 70°C. A reverse happens during cooling.

Output Power of OTEH

The output power of the engine is computed as:

$$Power=\frac{2}{m}\left(1-b/b_2\right)\left(\frac{L_{AB}(T_c)G(T_{heating})}{n_1}-\frac{L_{CD}(T_c)G(T_{cooling})}{n_1}\right)^2\left(\frac{(d_w)^4)}{8(D_s)^3 n_2}\right)^2 t \quad (41)$$

Efficiency of the Engine

The engine efficiency is calculated as:

Abu-Kharma M, Int J Plant Anim Environ Sci 2024
DOI:10.26502/ijpaes.4490161

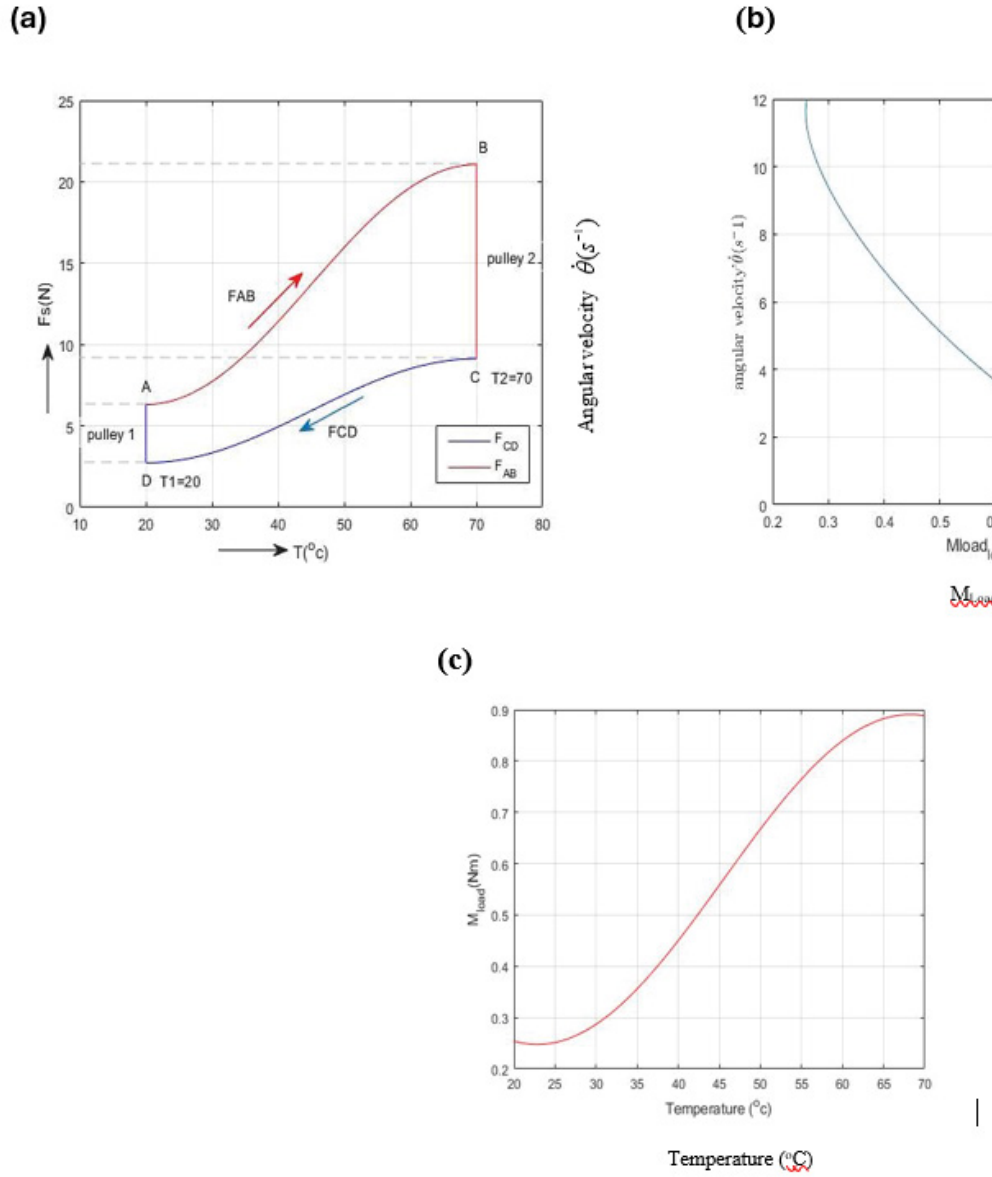

Figure 2: simulation of result (a) forces during heating and cooling versus temperature (b) moment versus temperature, (c) rotation rate versus output torque at pulley 1 for heating chamber.

$$Q_{in} = \int_0^{\tau} \left[\frac{2\pi (R_w H_h (T_w - T(t))}{m'} \right] dt \quad (42)$$

$$W = P_{spec} \times t \quad (43)$$

$$P_{spec} = \frac{P_{total}}{m_{total}} \quad (44)$$

$$P_{total} = M_{load} \times \dot{\theta} \quad (45)$$

$$m_{total} = m'l \quad (46)$$

$$l = 2\pi R_S n$$

$$\eta = \frac{W}{Q_{in}} \quad (47)$$

$$\eta = \frac{\frac{2}{m}\left(1 - b_1/b_2\right)\left(\frac{L_{AB}(T_c)G(T_{heating})}{n_1} - \frac{L_{CD}(T_c)G(T_{cooling})}{n_1}\right)^2 \left(\frac{(d_w)^4}{8(D_s)^3 n_2}\right)^2 t}{\int_0^{\tau}\left[\frac{2\pi(R_w H_h (T_w - T(t))}{m'}\right] dt} \quad (48)$$

Where R_w is wire radius; R_S is SMA spring radius; m_{total} is the total mass; m' is the wire linear density; l is SMA spring current length; H_h is the convection heat transfer coefficient for heating, τ is the total time taken; P_{total} is the total power produced; P_{spec} is the specific power.

Using parameters from Table 1, the following simulations are performed:

Fitting

The behavior of the SMA spring of (x-T) is modeled using Eq. 49.

Abu-Kharma M, Int J Plant Anim Environ Sci 2024
DOI:10.26502/ijpaes.4490161

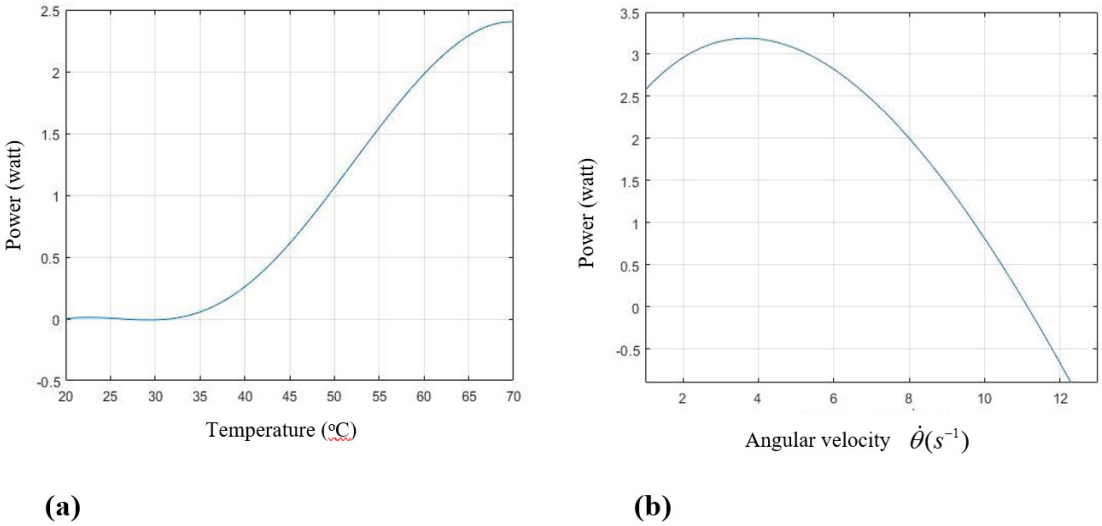

Figure 3: Simulation of power (a) verse temperature (b) verse angular velocity.

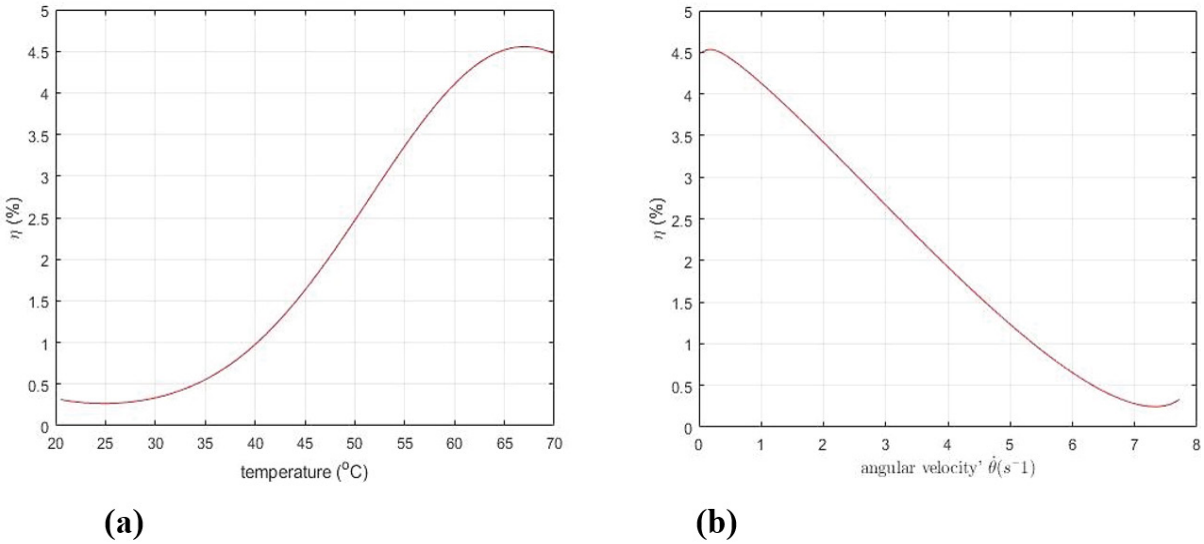

Figure 4: Simulation of efficiency (a) versus temperature (b) versus angular speed.

$$T(x) = T_0 - \pi T_1 [\frac{x - x_0}{x_M - x_A}] \csc [\frac{x - x_A}{x_M - x_A}] \quad (49)$$

$$T(x,F) = T_0(F) - \pi T_1(F) \left[\frac{x - x_A(F) - x_{0(F)}}{x_M(F) - \Pi_A(F)}\right] \csc \left[\frac{x(F) - x_A(F)}{x_M(F) - x_A(F)}\right] \quad (50)$$

Where T_0, T_1, x_0, x_A, x_M are obtained from the experiment, x_A, x_M are austenite and martensite stretch ratios. T_0, T_1, and x_0 are also parameters for shaping and positioning. The equation above will simulate the behavior of the SMA spring under the influence of temperature change. Using the estimated parameters, the following simulations are performed:

Experiment

The NiTi SMA heat engine prototype shown in Figure 6 was tested, and it developed at 110 rpm at 70°C. In real practice, when the engine is used for geothermal energy conversion, the water temperature may be up to 90°C. But when the engine is used for ocean thermal energy conversion, the seawater will be further heated up to a sufficient temperature using a solar heater. The arrangement of the NiTi SMA heat engine after construction is shown in Figure 7, and a series of experiments were conducted.

Comparison Between Experimental and Simulated Data

Using the experimental data and the parameters from Table 1, the moment generated is plotted in Figure 7 (a), and the angular speed versus moment in Figure 7(b).

Abu-Kharma M, Int J Plant Anim Environ Sci 2024
DOI:10.26502/ijpaes.4490161

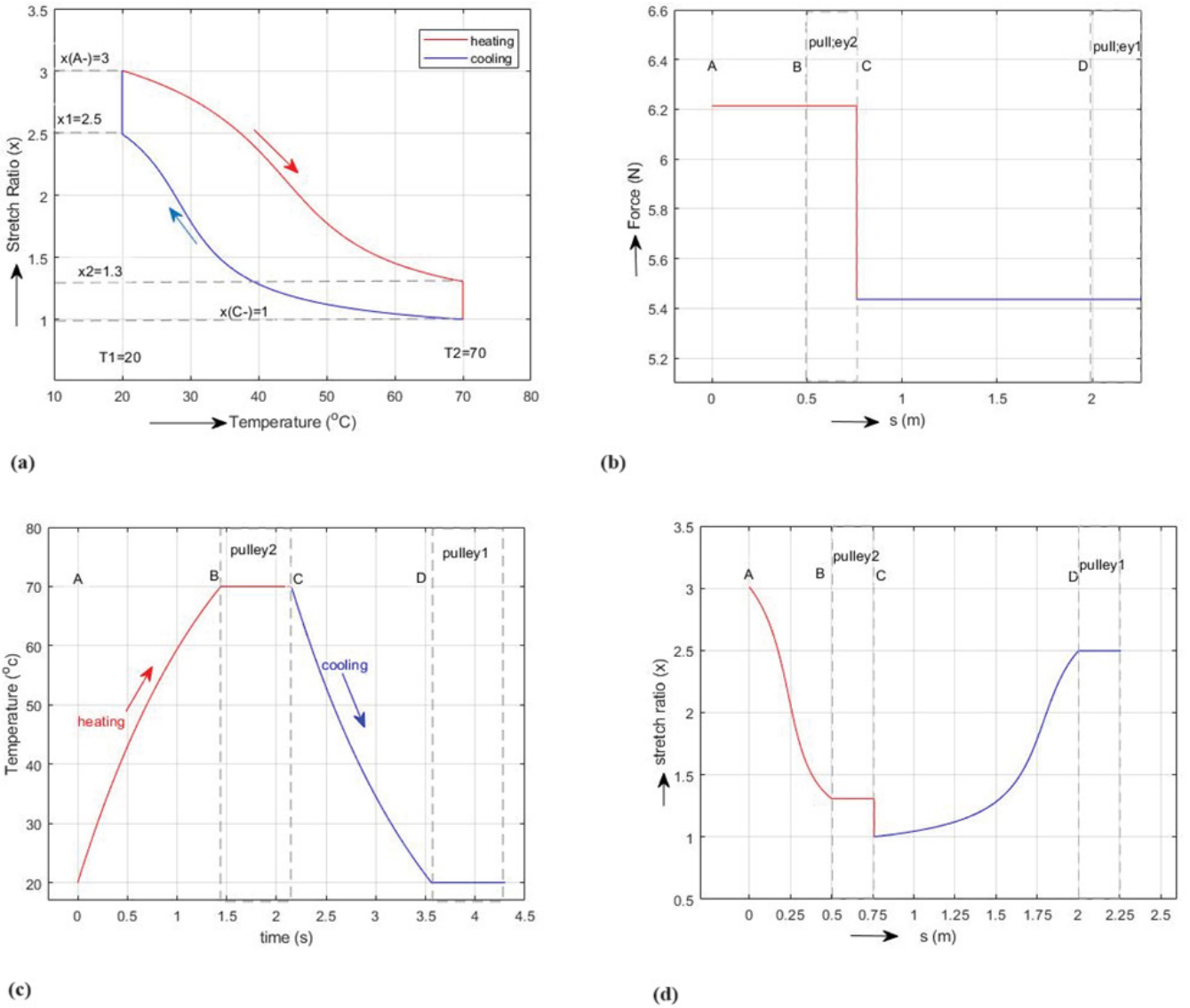

Figure 5: (a) stretch ratio verse temperature (b) simulation of force (c) temperature versus time (d) stretch ratio distributions along the SMA spring loop.

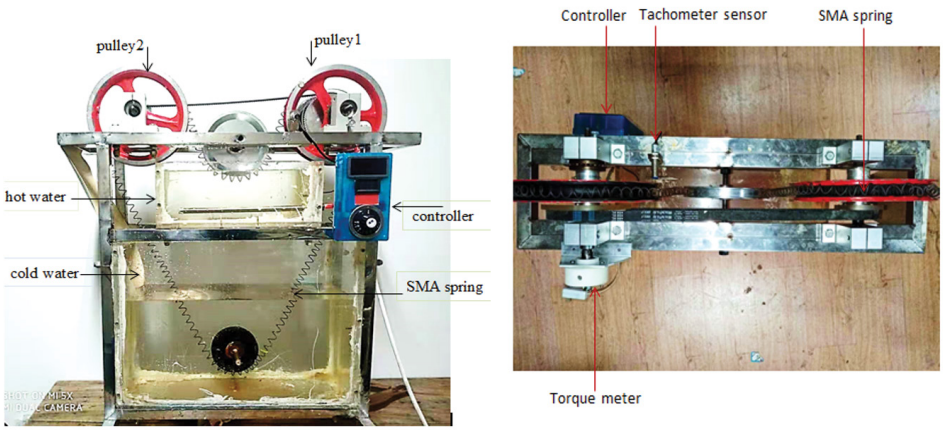

Figure 6: The SMA heat engine.

Citation: Rabiu Ahamd Abubakar, Nuhu Ibrahim. Thermal Energy Conversion Using NITI Shape Memory Alloy Material. International Journal of Plant, Animal and Environmental Sciences.14 (2024): 20-30.

Abu-Kharma M, Int J Plant Anim Environ Sci 2024
DOI:10.26502/ijpaes.4490161

Table 1: Simulation parameter for Ti-49, 51Ni SMA material is used in this OTEH.

	Parameter description	Value	unit
a	Pulley 1&2 radius	100	mm
b_1	Timing pulley 1 diameter	115	mm
b_2	Timing pulley 2 diameters	57	mm
x	Stretch ratio	1:3	-
For heating			
x_A	Austenite stretch ratio	0.9517	-
x_M	Martensite stretch ratio	3.6960	-
x_o	Initial stretch ratio	1.7564	-
To	Initial Temperature	50.5161	°C
T_1	Temperature 1	15.0585	°C
For cooling			
x_A	Austenite stretch ratio	0.8307	-
x_M	Martensite stretch ratio	3.0646	-
x_o	Initial stretch ratio	1.9245	-
To	Initial Temperature	28.5901	°C
T_1	Temperature 1	7.6448	°C
D	SMA spring diameter	16	mm
G_M	Martensite shear modulus	7.5×10^9	pa
G_A	Austenite shear modulus	7.5×10^9	
A_S	Austenite start	20	°C
A_f	Austenite finish	70	°C
Ms	Martensite start	73	°C
Mf	Martensite finish	15	°C
H_h	Convection heat transfer coefficient for heating	1500	W/ ($m^{2o}C$)
Hc	Convection heat transfer coefficient for cooling	270	W/($m^{2o}C$
m'	Wire linear mass density	0.455	g/m
m_p	Mass of the pulley1	62.59	g
Tc	Coldwater temperature	20	°C
T_h	Hot water temperature	70	°C
n	Number of turns	262	nil
δ_L	displacement	258×10^{-3}	mm
D	SMA spring diameter	16×10^{-3}	mm
d	SMA wire diameter	1.5×10^{-3}	mm
ϕ	wrap angle	150°	
C_s	SMA Specific heat	0.63	J/(g °C)
L_{AB}	Length of AB distance	500	mm
L_{CD}	Length of CD distance	1300	mm

Abu-Kharma M, Int J Plant Anim Environ Sci 2024
DOI:10.26502/ijpaes.4490161

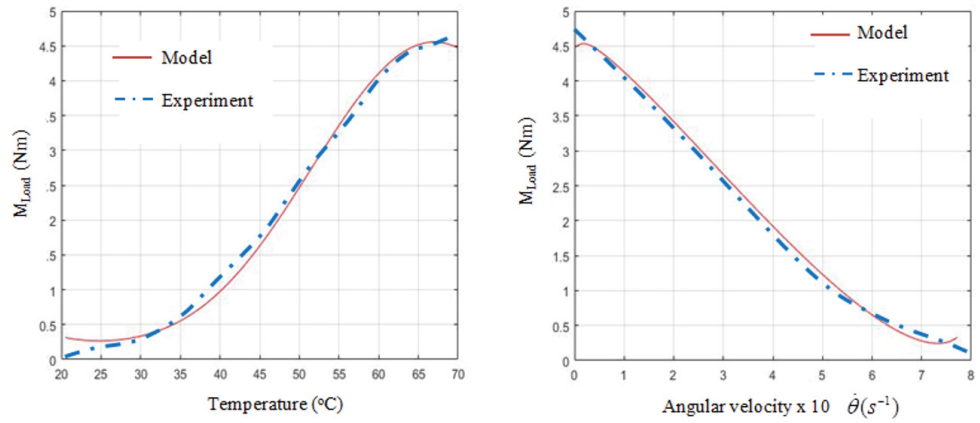

(a) **(b)**

Figure 7: (a) moment versus temperature (b) rotation rate versus output torque at pulley 1.

Discussion

Figure 2 (a) shows the simulation of force verse temperature during cooling and heating processes. It shows that the relationship is a nonlinear one. Figure 2 (b) simulates the torque generated by the engine with maximum torque of 0.9 Nm at the corresponding zero value of angular velocity. And also, it is a nonlinear one. Figure 3 (a) shows the graph of power versus temperature. As heating starts, there is zero power until after the critical phase transformation temperature of (30°C). Power then increases with temperature change with a nonlinear relationship. Figure 3 (b) represents the simulation of power versus angular speed. The curve goes with a nonlinear relationship for a maximum power of 3.2 watts at 3.2 revolutions per second, then decreases. Figure 4 (a) demonstrates the thermodynamic engine efficiency as a function of temperature, and in Figure 7 (b) as a function of rotation speed which is a nonlinear curve. Figure 5 represents the simulation of stretch ratio as a function of temperature for the full engine operation cycle. The graph forms a hysteretic one. Figure 6 (b) shows the force along the SMA spring loop. It indicates that there is a constant force between the two active pulleys. Figure 5 (c) shows the stretch ratio as a function of time, and Figure 5 (d) shows the stretch ratio distributions along the spring length. Both two graphs show a nonlinear nature. Figure 7 represents a comparison between model and experimental data. There is good fitting in both (a) and (b).

Conclusion

A heat engine based on NiTi SMA is designed, modeled, constructed and tested. The simulated data are compared with the experimental one with good fitting. The engine developed a power of 2.4 watts, with maximum efficiency of 4.51 %. This shows that the engine can harvest both ocean thermal and geothermal energy.

Declarations

Availability of data and materials: Not applicable

Competing interests: Ocean thermal energy conversion

Funding: Chineese government Scholarship (CSC)

Authors' contributions

Modeling of Ocean thermal energy Harvester

Acknowledgements

I sincerely express my appreciation and gratitude to the Chinese Scholarship Council (CSC) for its sponsorship to accomplish this program.

References

1. Lyu W, Pu H, Xiao H, et al. Thermal Performance of Energy Pile with Deeply Penetrating 1-U-Shape Heat Exchanger. Geothermics 91 (2021): 102023.
2. Abdelsalam MY, Teamah HM, Lightstone MF, et al. Hybrid Thermal Energy Storage with Phase Change Materials for Solar Domestic Hot Water Applications: Direct versus Indirect Heat Exchange Systems. Renewable Energy 147 (2020): 77-88.
3. Giostri A, Binotti M, Sterpos C, et al. Small Scale Solar Tower Coupled with Micro Gas Turbine. Renewable Energy 147 (2020): 570-83.
4. Fitts CR. Groundwater Science Subsurface Heat Flow and Geothermal Energy (2013).
5. Li H, Sham R, Zhibin Y, et al. An Inverse Mean-Line Design Method for Optimizing Radial Outflow Two-Phase Turbines in Geothermal Systems. Renewable Energy 168 (2021): 463-90.
6. Ma Z, Yanhui W, Shuxin W, et al. Ocean Thermal Energy

Harvesting with Phase Change Material for Underwater Glider. Applied Energy 178 (2016): 557-66.

7. Zhao C, Qiao X, Cao Y, et al. Application of Hydrogen Peroxide Presoaking prior to Ammonia Fiber Expansion Pretreatment of Energy Crops. Fuel 205 (2017): 184-91.
8. Qiao X, Zhao C, Shao Q, et al. Structural Characterization of Corn Stover Lignin after Hydrogen Peroxide Presoaking prior to Ammonia Fiber Expansion Pretreatment. Energy and Fuels 32 (2018): 6022-30.
9. Zhao C, Qiao X, Shao Q, et al. Synergistic Effect of Hydrogen Peroxide and Ammonia on Lignin. Industrial Crops and Products 146 (2020): 112177.
10. Ahmad SK, Faisal H. Maximizing Energy Production from Hydropower Dams Using Short-Term Weather Forecasts. Renewable Energy 146 (2020): 1560-77.
11. Gil-gonzález W, Oscar DM, Alejandro G. Modeling and Control of a Small Hydro-Power Plant for a DC Microgrid. Electric Power Systems Research 180 (2020): 106104.
12. Cao D, Hu W, Xu X, et al. Bidding Strategy for Trading Wind Energy and Purchasing Reserve of Windpower producer–A DRL Based Approach. Electrical Power and Energy Systems 117 (2020): 105648.
13. Al-Iedani I, Zoran G. Order Reduction of a Wind Turbine Energy System via the Methods of System Balancing and Singular Perturbations. Electrical Power & Energy Systems 117 (2020): 1056.
14. Huang W, Zheng D, Chen X, et al. Standard Thermodynamic Properties for the Energy Grade Evaluation of Fossil Fuels and Renewable Fuels. Renewable Energy 147 (2020): 2160-70.
15. Obuz S, Ayar M, Trevizan RD, et al. Renewable and Energy Storage Resources for Enhancing Transient Stability Margins : A PDE-Based Nonlinear Control Strategy,. Electrical Power and Energy Systems 116 (2020): 105510.
16. Østergaard PA, Duic N, Noorollahi Y, et al. Sustainable Development Using Renewable Energy Technology. Renewable Energy 146 (2020): 2430-37.
17. Rahman, MM, Velayutham E. Renewable and Non-Renewable Energy Consumption-Economic Growth Nexus : New Evidence from South Asia. Renewable Energy 147 (2020): 399-408.
18. Salehi A, Mousavi SM, Fasihfar A, et al. Energy, Exergy, and Environmental (3E) Assessments of an Integrated Molten Carbonate Fuel Cell (MCFC), Stirling Engine and Organic Rankine Cycle (ORC) Cogeneration System Fed by a Biomass-Fueled Gasifier. International Journal of Hydrogen Energy 44 (2019): 31488-505.
19. Emeksiz C, Bahattin D. The Determination of Offshore Wind Energy Potential of Turkey by Using Novelty Hybrid Site Selection Method. Sustainable Energy Technologies and Assessments 36 (2019): 100562.
20. Urbanucci L, Testi D. Integration of Reversible Absorption Heat Pumps in Cogeneration Systems: Exergy and Economic Assessment. Energy Conversion and Management 200 (2019): 112062.
21. Herzog AV, Lipman TE, Daniel MK. Renewable Energy Sources. Energy and Resources Group Renewable and Appropriate Energy Laboratory (2001).
22. Herzog AV, Lipman TE, Edwards JL, et al. Renewable Energy: A Iable Choice. Environment 43 (2001): 43-47.
23. Kaya O, Anna MK, Wojciech JF. Achieving Renewable Energy, Climate, and Air Quality Policy Goals: Rural Residential Investment in Solar Panel. Journal of Environmental Management 248 (2019): 109309.
24. Yamada N, Hoshi A, Yasuyuki I. Performance Simulation of Solar-Boosted Ocean Thermal Energy Conversion Plant. Renewable Energy 34 (2009): 1752-58.
25. Etemadi A, Arash E, Orang AA, et al. Electricity Generation by the Ocean Thermal Energy. Energy Procedia 12 (2011): 936-43.
26. Finney KA. Ocean Thermal Energy Conversion. Internation Journal of Trend in Scientific Research and Development 1 (2008): 17-23.
27. Dhunny AZ, Allam Z, Lobine D, et al. Sustainable Renewable Energy Planning and Wind Farming Optimization from a Bio-Diversity Perspective. Energy 185 (2019): 1282-97.
28. De Vrieze J, Verbeeck K, Pikaar I, et al. The Hydrogen Gas Bio-Based Economy and the Production of Renewable Building Block Chemicals, Food, and Energy. New Biotechnology 55 (2020): 12-18.
29. Wang H, Lei Z, Zhang X, et al. A review of deep learning for renewable energy forecasting. Energy Conversion and Management 198 (2019): 111799.
30. Masutani SM, Takahashi PK. Ocean Thermal Energy Conversion (OTEC). Encyclopedia of Ocean Sciences 1 (2010): 167-73.
31. Tanaka M, Saito K. Fundamental Study on Energy Conversion System Using Shape Memory Alloy. Journal of Mechanical Engineering Laboratory 47 (1993): 257-71.
32. Christopher CB, Arbor A, Browne AL. SMA Heat Engine: Advancing from a Scientific Curiosity to a Practical Reality. In: Smart Materials, Structures & NDT in Aerospace Conference, Montreal, Quebec, Canada: IZFP (2011): 1-6.

Abu-Kharma M, Int J Plant Anim Environ Sci 2024
DOI:10.26502/ijpaes.4490161

33. Schiller EH. Heat Engine Driven by Shape Memory Alloys : Prototyping and Design Heat Engine Driven by Shape Memory Alloys : Prototyping and Design." Virginia Polytechnic Institute and State University (2002).

34. Johnson AD. Memory Alloy Heat Engine and Method of Operation. Oakland, CA (1976).

35. Wakjira JF. Design "The VT1 Shape Memory Alloy Heat Engine Design. Virginia Polytechnic Institute and State University (2001).

36. Browne A. SMA Heat Engines: Advancing from a Scientific Curiosity to a Practical Reality. In: Smart Materials, Structures & NDT in Aerospace Conference (2011): 1-6.

37. Margvelashvili IG, Zviadadze M, Zamtaradze LA. The Efficiency and Power of the Martensite Rotor Heat Engine. I. Physics 1 (2012): 1-11.

38. Cisse C, Wael Z, Tarak B. A Review of Constitutive Models and Modeling Techniques for Shape Memory Alloys. International Journal of Plasticity 76 (2016): 244-84.

39. Lagoudas DC. Shape Memory Alloys: Modeling and Engineering Applications. New York: Springer (2008).

40. Zhou B, Kang Z, Wang Z, et al. Finite Element Method on Shape Memory Alloy Structure and its Applications. Chinese Journal of Mechanical Engineering 32 (2019): 84.

41. Malygin GA. The Mechanism of Influence of Dispersed Nanoparticles on Parameters of the Martensitic Transitions in Alloys with the Shape Memory Effect. Mechanical Properties, Physics of Strength, and Plasticity 61 (2019): 2083-89.